

Computational Neuroscience

Lipschitz-Killing curvature based expected Euler characteristics for p -value correction in fNIRS

Hua Li, Sungho Tak, Jong Chul Ye*

Bio Imaging and Signal Processing Lab., Dept. of Bio and Brain Engineering, KAIST, 373-1 Guseong-dong Yuseong-gu, Daejeon 305-701, Republic of Korea

ARTICLE INFO

Article history:

Received 15 March 2011

Received in revised form 9 September 2011

Accepted 18 October 2011

Keywords:

Near-infrared spectroscopy
Statistical parameter mapping
 t -Test
Family-wise error rate control
Expected Euler characteristics
Lipschitz-Killing curvature

ABSTRACT

Functional near-infrared spectroscopy (fNIRS) is a non-invasive imaging approach for measuring brain activities based on changes in the cerebral concentrations of hemoglobin. Recently, statistical analysis based on a general linear model (GLM) has become popular. Here, to impose statistical significance on the activation detected by fNIRS, family-wise error (FWE) rate control is important. However, unlike fMRI, in which measurements are densely sampled on a regular lattice and Gaussian smoothing makes the resulting random field homogeneous, the random fields from fNIRS are inhomogeneous due to the interpolation from sparsely and irregularly distributed optode locations. Thus, tube formula based correction has been proposed to address this issue. However, Sun's tube formula cannot be used for general random fields such as F -statistics. To overcome these difficulties, we employ the expected Euler characteristic approach based on Lipschitz-Killing curvature (LKC) to control the family-wise error rate. We compared this correction method with Sun's tube formula for t -statistics to confirm the existing method. Based on this comparison, we show that covariance estimation should be modified to consider channel-wise least-square residual correlation. These new results supplement the existing tool of statistical parameter mapping for fNIRS.

© 2011 Elsevier B.V. All rights reserved.

1. Introduction

Functional near-infrared spectroscopy (fNIRS) is a non-invasive imaging approach for detecting brain activity via changes in the cerebral concentrations of oxy-hemoglobin (HbO) and deoxy-hemoglobin (HbR) through the “therapeutic optical window” between 650 to 950 nm (Villringer and Dirnagl, 1995; Boas et al., 2001; Cope and Delpy, 1988). Unlike other non-invasive imaging approaches, such as functional magnetic resonance imaging (fMRI) and positron emission tomography (PET), fNIRS can directly measure hemodynamic parameters, such as HbO, HbR, and total hemoglobin (HbT), at a high temporal resolution under the hypothesis of constant hematocrit. In addition, fNIRS is also very useful in examining patients and children who might not tolerate the confined environments of fMRI (Schroeter et al., 2004). Moreover, since an fNIRS system is compact, portable, and inexpensive, it has great potential for routine monitoring and many other applications.

However, its spatial resolution is low and it lacks anatomical information. Since fMRI has high spatial resolution and exact anatomical information, combined fNIRS and fMRI is very powerful to detect brain activity. For example, Boas et al. (2003), Toronov et al. (2001) and Mehagnoul-Schipper et al. (2002) studied the

temporal dynamics of HbO, HbR, and HbT to show that HbR correlated with BOLD signal; Ye et al. (2009) used fMRI as ground truth to perform receiver operating characteristic (ROC) analysis of fNIRS.

Recently, to analyze fNIRS data, statistical analysis based on a general linear model (GLM) has become popular (Schroeter et al., 2004; Plichta et al., 2007; Koh et al., 2007; Ye et al., 2009). Since fNIRS detects the brain activation in a way similar to fMRI, the GLM approach that has been established for fMRI (Friston et al., 2007) can be applied in fNIRS. Schroeter et al. (2004) shows that GLM can be used as the standard statistical approach for optical imaging data. More specifically, the model equation includes the observation data, the design matrix and the error term. The explanatory variables constitute the design matrix which encodes and quantifies our knowledge about how the expected signal was produced (Friston et al., 2007). The convolution of the stimulation protocol and hemodynamic response function (HRF) is used as a predictor (Plichta et al., 2007). Moreover, the latency and dispersion derivatives are modeled and considered as regressors in the design matrix to compensate for individual and oxygen species specific hemodynamic variation.

For parameter estimation, either ordinary least-square (OLS) or generalized least-square estimation (GLS) is often used. For inference, a voxel-wise statistical test (i.e., t - or F -test) constructs the statistical map, and then a threshold is determined to detect the activation map for a given p -value. Either an uncorrected or a corrected p -value is often applied to determine a threshold. However,

* Corresponding author. Tel.: +82 042 350 4320.

E-mail address: jong.ye@kaist.ac.kr (J.C. Ye).

an uncorrected p -value only controls the type I error for each voxel independently. Since there are many voxels in the search volume, we are interested to control the type I error for the whole search volume. This procedure is called family-wise error rate control.

For p -value correction, there are several approaches. If all the voxels in the search volume are independent, Bonferroni correction is a very simple and direct method to solve this problem. However, spatial correlation is very common in functional imaging, so Bonferroni correction often leads to overly conservative results (Friston et al., 2007). Other methods such as false discovery rate (FDR) (Singh and Dan, 2006) can be used. For family-wise error rate control, this problem can be addressed by the expected Euler characteristic (EC) method. The Euler characteristic is a geometric property of a 3D volume which can be calculated as the number of connected excursion set minus the number of holes plus the number of hollows (Worsley, 1995). When the threshold is high enough, the number of blobs is one or zero. Thus, the expected EC represents the probability of finding an above threshold blob; hence, the expected EC is approximately equivalent to the probability of family-wise error (Friston et al., 2007).

For PET data or smoothed fMRI, it is reasonable to assume that the noise component of image data is homogeneous, so the theoretical results for the p -value of local maxima and the size of supra-threshold clusters of a statistical parametric map (SPM) based on random field theory can be used (Worsley et al., 1999). However, fNIRS data is inhomogeneous, where the full width at half maximum (FWHM) is not same in all directions and across all voxels in the image due to the interpolation from sparsely and irregularly distributed optode locations, so the expected EC method for homogeneous random field is not suitable. To address this problem, Ye et al. (2009) applied Sun's tube formula to control the family-wise error rate for individual analysis, since the degree of freedom in fNIRS time series is large enough to approximate the individual t random field as a Gaussian random field. The p -value correction method has been implemented in a statistical parameter mapping toolbox for NIRS (NIRS-SPM) (<http://bisp.kaist.ac.kr/NIRS-SPM.html>).

Recently, to address shape analysis in brain imaging, an expression of the excursion probability for general inhomogeneous fields on manifolds has been developed by using Lipschitz-Killing curvatures (LKC) and the kinetic fundamental formulas by warping the random field into a space such that the resulting random fields are homogeneous (Worsley et al., 1999). Here, we term this approach as LKC-based expected EC. LKC is a measure of the intrinsic volume of a search volume in the Riemannian metric defined by the variogram (Taylor and Worsley, 2008). This LKC-based expected EC method can solve the p -value correction problem even for the case of the inhomogeneous random field. Hence, the LKC-based expected EC method provides the solution to the family-wise error rate control in fNIRS that has an inhomogeneous random field due to the inhomogeneous interpolation kernel. Furthermore, one advantage of the Euler characteristic method over the tube formula is that it can be applied to non-Gaussian fields such as t and F random fields. Hence, this formula can be applied for both individual and group analyses of fNIRS.

One of the main contributions of this paper is to verify the accuracy of existing Sun's tube formula in NIRS-SPM (Ye et al., 2009) for p -value correction of an individual t field using LKC-based expected EC. We show that the geometric terms \mathcal{L}_2 in EC and κ_0 in the tube formula are identical for the case of independent channel residuals in fNIRS, but if the channel residuals are correlated, the value of \mathcal{L}_2 is smaller than κ_0 . However, by incorporating channel-wise least-square residual correlation into channel-residual covariance, we can verify that the geometric terms \mathcal{L}_2 and κ_0 become identical. The results indicates one important finding that is unique for fNIRS analysis. More specifically, in fMRI, the method of

estimating the covariance at each voxel is based on restricted maximum likelihood (ReML), and the variance term at each voxel is estimated independently using the usual estimator in a least-square mass-univariate scheme (Friston et al., 2007). There is no need to use the covariance matrix of all voxels to calculate the variance term. However, in fNIRS, there are only a few measurement channels, and the other voxels are interpolated, so the variance term at each interpolated voxel is calculated using the channel-residual covariance. In NIRS-SPM, the channel-residual covariance is calculated with the assumption that there is no spatial correlation between different channel residuals. However, we found that the channel-wise least-square residual correlation does exist and we need to take this term into account in calculating the t - and F -statistics. We show that this also removes the artifacts in individual t maps that are often observed from optode placements. The results in this paper supplement existing statistical analysis in fNIRS by filling the missing components of the toolbox. The new components will be included in the next release of NIRS-SPM which can be downloaded from the authors' homepage. (<http://bisp.kaist.ac.kr/NIRS-SPM.html>)

2. Theory

In this section, we will review the LKC-based expected Euler characteristic and Sun's tube formula for p -value correction, respectively.

2.1. LKC-based expected EC

At a high threshold, the expected EC is approximately equivalent to the probability of a family-wise error (Friston et al., 2007). For an inhomogeneous random field $Z(r)$ on a manifold Φ , the expected EC of excursion set $A_t \equiv A_t(Z, \Phi) = \{r \in \Phi : Z(r) \geq t\}$ at high threshold t is given by Taylor and Worsley (2008):

$$P\left(\sup_{r \in \Phi} Z(r) \geq t\right) \approx E(\varphi(A_t)) = \sum_{d=0}^D \mathcal{L}_d(\Phi) \rho_d(t), \quad (1)$$

where $\mathcal{L}_d(\Phi)$ is Lipschitz-Killing curvatures (LKC) of the manifold Φ representing the intrinsic volume of Φ in a Riemannian metric, and $\rho_d(\cdot)$ denotes the d -dimensional EC density function determined by the type of random fields (Taylor and Worsley, 2008). For Gaussian random fields, the EC density function is represented by a Hermite polynomial (Adler and Taylor, 2007), and for general non-Gaussian random fields, the so-called kinetic fundamental formula provides the explicit representation.

For a Gaussian random field $Z(r)$, an excursion probability using the volume of the tube formula is basically the same as Eq. (1), except for the zero-th order EC density function $\rho_0(u)$ (See Theorem 10.6.1 in Adler and Taylor (2007)). In particular, the calculation of the LKC can be done explicitly with respect to the basis functions of a finite term Karhunen-Loève expansion (Adler and Taylor, 2007). Based on the observation that the t -field can be approximated as a Gaussian random field which possesses a finite Karhunen-Loève expansion, Ye et al. (2009) were able to provide a close form expression of the dominant LKC term in the tube formula. However, for general statistics in both individual and group analysis, the general LKC-based expected EC formula in Eq. (1) is more appropriate and should be exploited.

A method to estimate LKC was developed by Worsley et al. (1999) and Taylor and Worsley (2007), and we review it here briefly. The least-square residual $\mathbf{r}(r) \in \mathbb{R}^N$ of a general linear model is:

$$\mathbf{r}(r) = \mathbf{y}(r) - \mathbf{X}\mathbf{X}^T \mathbf{y}(r), \quad (2)$$

where $\mathbf{y}(r) \in \mathbb{R}^N$ are the measurement times series, \mathbf{X} is the design matrix and \dagger is the Moore-Penrose pseudoinverse of a matrix. Then, the corresponding normalized residual is:

$$\mathbf{Q}(r) = \frac{\mathbf{r}(r)}{\|\mathbf{r}(r)\|_2} \in \mathbb{R}^N.$$

Let

$$\mathbf{S}(r) = (\mathbf{Q}(r + \delta_1) - \mathbf{Q}(r), \dots, \mathbf{Q}(r + \delta_D) - \mathbf{Q}(r)) \in \mathbb{R}^{N \times D}, \quad (3)$$

where δ_k is the D -dimensional vector of zeros with k th component equal to the unit step size along the lattice axis $k, k = 1, \dots, D$. In fNIRS topography mapping, the dimension is $D = 2$. (For a tomographic mapping, $D = 3$.) Then, the 2-dimensional LKC of Φ can be estimated as:

$$\hat{\mathcal{L}}_2(\Phi) = \sum_{r \in \Phi} \det(\mathbf{S}(r) \mathbf{S}(r))^1/2, \quad (4)$$

where $\det(\cdot)$ denotes the determinant. Estimating the lower dimensional LKC is more complicated, so a short-cut method is often used in practice. Specifically, the D -dimensional LKC, which makes the largest contribution to the p -value approximation, is first estimated. Then, the lower dimensional terms are estimated by simply assuming that Φ is a D -dimensional ball (Taylor and Worsley, 2008). In fNIRS topographic mapping, the dimension is $D = 2$; therefore, we assume that Φ is a disk, and then a short-cut calculation of $\hat{\mathcal{L}}_1(\Phi)$ and $\hat{\mathcal{L}}_0(\Phi)$ can be calculated as:

$$\hat{\mathcal{L}}_0(\Phi) = 1, \quad \hat{\mathcal{L}}_1(\Phi) = \pi r, \quad (5)$$

where $r = \sqrt{\hat{\mathcal{L}}_2(\Phi)/\pi}$. In applying LKC-based expected EC for fNIRS, Eq. (3) can be calculated with respect to the interpolation kernel used in fNIRS topographic mapping, as shown in Appendix A.

2.2. Sun's tube formula

In order to explain tube-based p -value correction, let us first review the individual analysis. Note that the individual-level GLM for the l -th subject at any position $r \in \Phi$ can be written as follows (see Appendix B):

$$\mathbf{y}_l(r) = \mathbf{X} \alpha_l(r) + \epsilon_l(r), \quad (6)$$

where $\mathbf{y}_l(r)$ is an N -dimensional time series at the interpolated position $r \in \Phi$, \mathbf{X} is an individual-level design matrix, and $\alpha_l(r)$ is an individual-level response parameter which quantifies the contribution of each regressor, $\epsilon_l(r)$ is a vector representing the error term.

Using the ordinary least square (OLS) approach, we can estimate the individual-level parameter $\hat{\alpha}_l(r)$ and its covariance as:

$$\hat{\alpha}_l(r) = \mathbf{X}^\dagger \mathbf{y}_l(r) \in \mathbb{R}^M, \quad \mathbf{C}_{\hat{\alpha}_l}(r) = \mathbf{X}^\dagger \mathbf{C}_{\epsilon_l}(r) \mathbf{X}^{\dagger T} \in \mathbb{R}^{M \times M}, \quad (7)$$

where $\mathbf{C}_{\epsilon_l}(r)$ is the estimation of temporal noise covariance at the interpolated position r . Then, the individual t -statistic can be calculated as follows (Ye et al., 2009):

$$T_l(r) = \frac{\hat{\lambda}_l(r)}{\sqrt{\mathbf{C}_{\hat{\lambda}_l}(r)}}, \quad (8)$$

where

$$\hat{\lambda}_l(r) = \mathbf{c}^T \hat{\alpha}_l(r) = \mathbf{c}^T \mathbf{X}^\dagger \mathbf{y}_l(r) \quad (9)$$

$$\begin{aligned} \mathbf{C}_{\hat{\lambda}_l}(r) &= \mathbf{c}^T \mathbf{C}_{\hat{\alpha}_l}(r) \mathbf{c} \\ &= \mathbf{c}^T \mathbf{X}^\dagger \mathbf{C}_{\epsilon_l}(r) \mathbf{X}^{\dagger T} \mathbf{c} \\ &= (\mathbf{b}(r)^T \boldsymbol{\Sigma}_l \mathbf{b}(r)) (\mathbf{c}^T \mathbf{X}^\dagger \mathbf{A}_l \mathbf{X}^{\dagger T} \mathbf{c}), \end{aligned} \quad (10)$$

where $\mathbf{c} \in \mathbb{R}^M$ denotes the contrast vector and \mathbf{A}_l is the temporal correlation, $\mathbf{C}_{\epsilon_l}(r) = (\mathbf{b}(r)^T \boldsymbol{\Sigma}_l \mathbf{b}(r)) \otimes \mathbf{A}_l$ as shown in Appendix B,

$\mathbf{b}(r)$ denotes the interpolation kernel, and $\boldsymbol{\Sigma}_l$ is channel-residual covariance (Ye et al., 2009):

$$\boldsymbol{\Sigma}_l = \begin{bmatrix} \sigma_l^{(1)2} \mathbf{O} & \dots & \mathbf{O} \\ \mathbf{O} & \sigma_l^{(2)2} \dots & \mathbf{O} \\ \vdots & \vdots & \ddots \\ \mathbf{O} & \mathbf{O} & \dots & \sigma_l^{(K)2} \end{bmatrix} \in \mathbb{R}^{K \times K}, \quad (11)$$

with variance of each channel:

$$\sigma_l^{(i)2} = \frac{\mathbf{y}_l^{(i)T} \mathbf{R}_X \mathbf{y}_l^{(i)}}{\text{trace}(\mathbf{R}_X \mathbf{A}_l)},$$

and the variance of interpolated voxel is:

$$\sigma_l(r)^2 = \mathbf{b}(r)^T \boldsymbol{\Sigma}_l \mathbf{b}(r).$$

In fMRI, the variance of each voxel is calculated directly using the voxel-wise residuals. However, in fNIRS, the variance of each voxel is obtained using the covariance of optode-channel measurement due to the interpolation. In NIRS-SPM, the channel-residual covariance is calculated with assumption that there is no spatial correlation between different channel residuals. In this paper, we will modify this term to consider the spatial correlation between different channel residuals. Therefore the (i, j) -th element of the $\boldsymbol{\Sigma}_l$ is calculated as follows:

$$\sigma_l^{(ij)2} = \frac{\mathbf{y}_l^{(i)T} \mathbf{R}_X \mathbf{y}_l^{(j)}}{\text{trace}(\mathbf{R}_X \mathbf{A}_l)}, \quad (12)$$

which will be shown to have great effect on the equivalence of Sun's tube formula and expected EC methods. The corresponding degree of freedom is:

$$df_l = \frac{\text{trace}(\mathbf{R}_X \mathbf{A}_l)^2}{\text{trace}(\mathbf{R}_X \mathbf{A}_l \mathbf{R}_X \mathbf{A}_l)}, \quad (13)$$

where $\mathbf{R}_X = \mathbf{I}_N - \mathbf{X} \mathbf{X}^\dagger$. In our actual experiment, for individual t field, the degree of freedom is around $df_l = 100$ for the case where the number of time points is $N = 5520$ and there are 26677 voxels interpolated from 24 channels.

For the case of the large degree of freedom in t statistic, it is well-known that t field can be approximated as Gaussian random field, so the tube formula has been derived as follows (for more detail, see Ye et al. (2009)):

$$P(\sup_{r \in \Phi} Z(r) \geq t) \approx \frac{\kappa_0}{2\pi^{3/2}} \Gamma\left(\frac{3}{2}\right) \left(1 - \Gamma\left(\frac{3}{2}, \frac{t^2}{2}\right)\right), \quad (14)$$

where

$$\kappa_0 = \sum_{r \in \Phi} \sqrt{|\det(\nabla \mathbf{u}(r) \nabla \mathbf{u}(r))|}, \quad (15)$$

$$\mathbf{u}(r) = \frac{\mathbf{C}_\beta^{1/2} (\mathbf{b}(r)^T \otimes \mathbf{I}_M) \mathbf{c}}{\sqrt{(\mathbf{b}(r)^T \boldsymbol{\Sigma}_l \mathbf{b}(r)) (\mathbf{c}^T \mathbf{X}^\dagger \mathbf{A}_l \mathbf{X}^{\dagger T} \mathbf{c})}}. \quad (16)$$

The formulae of Sun's tube formula (refer to Ye et al. (2009)) and LKC-based expected EC methods for 2-dimensional individual t maps are summarized in Table 1.

2.3. Comparison: EC vs. tube

Takemura and Kuriki (2002) have established that the tube formula and the Euler characteristic method give identical and valid asymptotic expansion of the tail probability of the maximum of a Gaussian random field when the random field has finite Karhunen-Loève expansion and the index set has positive critical radius (Takemura and Kuriki, 2003). However, this is based on an abstract

Table 1
Individual-level t -statistics.

LKC-based expected EC	Sun's tube formula
$P(\sup_{r \in \Phi} Z(r) \geq t) \approx \sum_{d=0}^D \mathcal{L}_d(\Phi) \rho_d(t)$	$P(\sup_{r \in \Phi} Z(r) \geq t) \approx \frac{\kappa_0}{2\pi^{3/2}} \Gamma\left(\frac{3}{2}\right) \left(1 - \Gamma\left(\frac{3}{2}, \frac{z^2}{2}\right)\right) \sim \kappa_0 \frac{1}{2\pi^{3/2}} z e^{-z^2/2}$
$\mathcal{L}_2(\Phi) = \sum_{r \in \Phi} \sqrt{ \det(\nabla \mathbf{Q}_l(r)' \nabla \mathbf{Q}_l(r)) }$	$\kappa_0 = \sum_{r \in \Phi} \sqrt{ \det(\nabla \mathbf{u}(r)' \nabla \mathbf{u}(r)) }$
$\mathbf{Q}_l(r) = \frac{\mathbf{r}(r)}{\ \mathbf{r}(r)\ }$	$\mathbf{u}(r) = \frac{\mathbf{c}^{1/2} (\mathbf{b}(r)^T \otimes \mathbf{I}_M) \mathbf{c}}{\sqrt{(\mathbf{b}(r)^T \Sigma_l \mathbf{b}(r)) (\mathbf{c}^T \mathbf{X}^T \mathbf{A}_l \mathbf{X}^T \mathbf{c})}}$
$\rho_2(t) = \frac{1}{2\pi^{3/2}} \frac{\Gamma((v+1)/2)}{(v/2)^{1/2} \Gamma(v/2)} \left(1 + \frac{t^2}{v}\right)^{-\frac{v+1}{2}}$	$\rho_2(z) = \frac{1}{2\pi^{3/2}} z e^{-(z^2/2)}$

mathematical setting, so we are interested in verifying this using real fNIRS data.

Note that Ye et al. (2009) only use the κ_0 term which is the most important constant from Weyl's formula (Ye et al., 2006). On the other hand, the LKC-based expected EC method includes \mathcal{L}_0 , \mathcal{L}_1 , and \mathcal{L}_2 , where \mathcal{L}_2 has largest contribution. By inspecting the formulae of these two methods, we find that κ_0 in the tube formula corresponds to \mathcal{L}_2 in the LKC-based expected EC method. Since the tube formula is restricted to Gaussian fields (Takemura and Kuriki, 2003), the other terms $1/(2\pi)^{3/2} z e^{-(z^2/2)}$ in tube formula corresponds to 2-dimensional EC density of Gaussian random field, whereas LKC-based expected EC method has the 2-dimensional EC density function for t -random field. This implies that there are two sources of differences between tube and EC. One for numerical differences in calculating κ_0 and \mathcal{L}_2 , and the other for the differences in the actual EC density functions. In this paper, we first compare \mathcal{L}_2 and κ_0 to show that the seemingly different two formulae provide the identical results. Then, as the degree of freedom becomes large, we show that the EC density functions for Gaussian and t provide similar threshold values.

3. Method

3.1. Behavior protocol

Right finger tapping (RFT) experiments were chosen to verify the validity of the proposed method. The experimental paradigm was composed of 21 s tapping and 30 s rest for each subject, which was repeated 10 times as shown in Fig. 1. The subject instruction was visually presented using a beam projector. When the word 'go' appeared, the subjects performed finger tapping with thumb and index finger repeatedly at a rate of about twice per second. When the word 'stop' appeared, the subjects stopped tapping and stared at a fixed point to avoid eye and head movements. The entire recording time was 552 s. The number of subjects was seven. The data were published by Ye et al. (2009). All subjects were right-handed and all had no history of neurological disease. Participants were given instructions regarding the experimental process of the NIRS and MRI, and all provided written informed consent. This study was approved by the Institutional Review Board of the Korea Advanced Institute of Science and Technology (KAIST).

3.2. Data acquisition

An NIRS instrument (Oxymon MK III, Artinis, the Netherlands) with 24 channels, 8 sources, and 4 detectors was used to measure the optical density variation at two wavelengths of 781 nm and 856 nm at a sampling frequency of 10 Hz. The system consists of the light source comprising a semiconductor, pulsed laser diodes (1 mW average laser power output), and the avalanche photo diode detector. A holder cap to fix the distance between the optodes was attached to the scalp around the primary motor cortex. The distance between the source and the detector was 3.5 cm. To ensure an accurate anatomical scanning session, T1-weighted structural images were acquired using a 3.0 T MRI system (ISOL, Republic of Korea).

3.3. Data analysis

After the data were acquired, we converted the optical densities to concentration changes of oxy- and deoxy-hemoglobin using the modified Beer–Lambert law (Cope and Delpy, 1988). The unit for the HbO and HbR concentration changes is μM . Since the differential pathlength factor is not obtainable in our continuous NIRS system, the value was assumed as four. We applied wavelet-MDL detrending (Jang et al., 2009) to remove the global drift, since this approach provides more consistent and reliable detrending results. As discussed in Section 2, for individual analysis, we used the NIRS–SPM toolbox to construct the individual t maps and used Sun's tube formula to do the p -value correction. We also controlled the family-wise error rate with the LKC-based expected EC and compared its result with that of the tube formula.

4. Experimental results

To compare the tube formula and the EC method, we first used simulation data to compare κ_0 and \mathcal{L}_2 . We constructed random Gaussian residuals with a length of $N=5384$ with variances equal to the real residual of HbO for each channel, and then calculated κ_0 and \mathcal{L}_2 , respectively. Recall that the channel-wise least-square residual time series refer Eq. (2), which corresponds to the time series after projecting the measurements to the null-space of the design matrix. In calculating κ_0 and \mathcal{L}_2 , we use the same interpolation kernel as in real data assuming the equivalent imaging geometry. The results show that $\kappa_0=50.54$ and $\mathcal{L}_2=50.87$, which

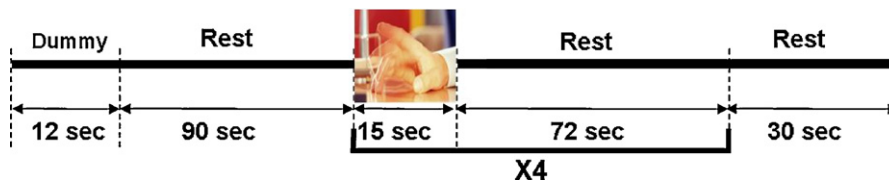


Fig. 1. Experimental paradigm.

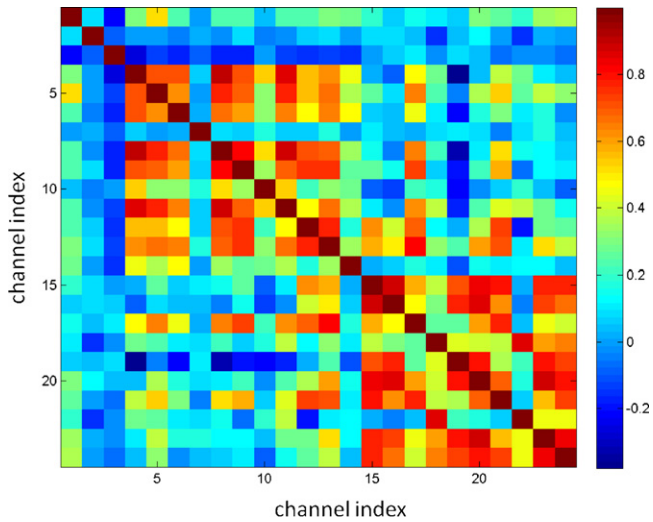


Fig. 2. Spatial correlation between least-square residuals from 24 channels in HbO measurements.

are nearly identical. However, when we use real HbO time series, we find that $\mathcal{L}_2 = 19.85$, whereas κ_0 remains the same. To explore the main causes of \mathcal{L}_2 decreasing, we first consider the temporal correlation Λ_l . We add the temporal correlation to the simulation data by smoothing and then calculate \mathcal{L}_2 again. However, the result is $\mathcal{L}_2 = 52.41$. Hence, the temporal correlation was not the cause. Next, we consider the spatial correlation. Fig. 2 shows the channel-wise spatial correlation structures of channel-wise least-square residual from real measurements. Real data shows significant spatial correlation between different channels, which may be due to a global trend or remaining activation patterns that cannot be removed by projecting to the null space of the design matrix. To verify that spatial correlation is the main cause, we added

Table 2
Values of \mathcal{L}_2 with respect to spatial correlation coefficient ρ .

ρ	\mathcal{L}_2
0	50.87
0.1	50.04
0.2	49.00
0.3	47.48
0.4	45.16
0.5	41.68
0.6	36.70
0.7	30.01
0.8	21.72
0.9	12.78

spatial correlations to the simulation data using AR(1) process across channels with parameter ρ . Table 2 summarizes the values of \mathcal{L}_2 for various ρ 's. We find that \mathcal{L}_2 decreases as the spatial correlation increases.

As described in Section 2, we then modify channel-residual covariance Σ_l by considering the spatial correlation between different channel residuals. After incorporating the $\sigma_l^{(ij)2}$ to the Σ_l , the result of the tube formula yields $\kappa_0 = 19.84$, which is basically same as $\mathcal{L}_2 = 19.85$. This indicates that whatever the reason for the spatial correlation in the least-square residuals, we should consider it to make the tube formula more accurate. In the following experiments, we modified NIRS-SPM to reflect this observation.

Next, we compare the thresholds produced by these two methods. The goal is to check the accuracy of Sun's tube formula which is based on approximating an individual t random field as a Gaussian random field. Since only the κ_0 term is used in Sun's tube formula, only \mathcal{L}_2 is included in the LKC-based expected EC method for a fair comparison. For the expected EC method, the EC density of t random field $\rho_2(t)$ is used, whereas the tube formula uses the EC density function of the Gaussian random field. Table 3 shows the thresholds for HbO, HbR, and HbT. As previously discussed, κ_0 and \mathcal{L}_2 are

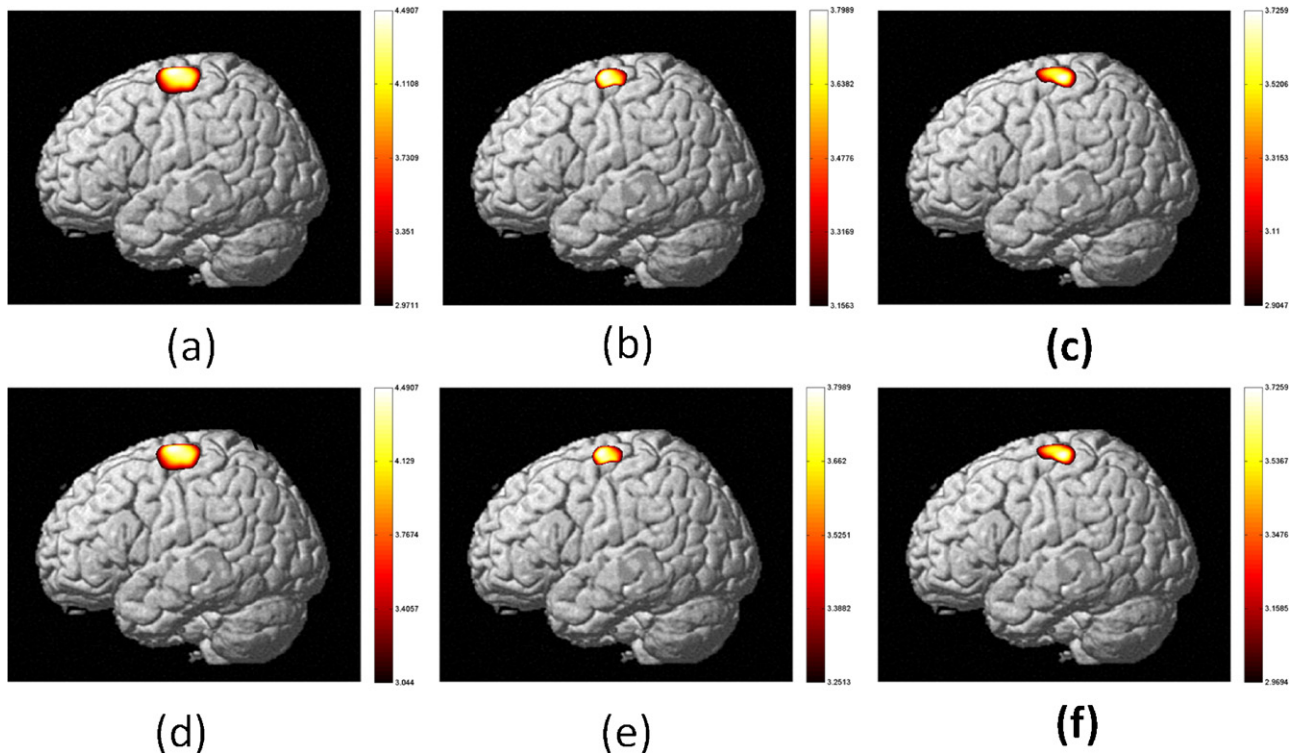
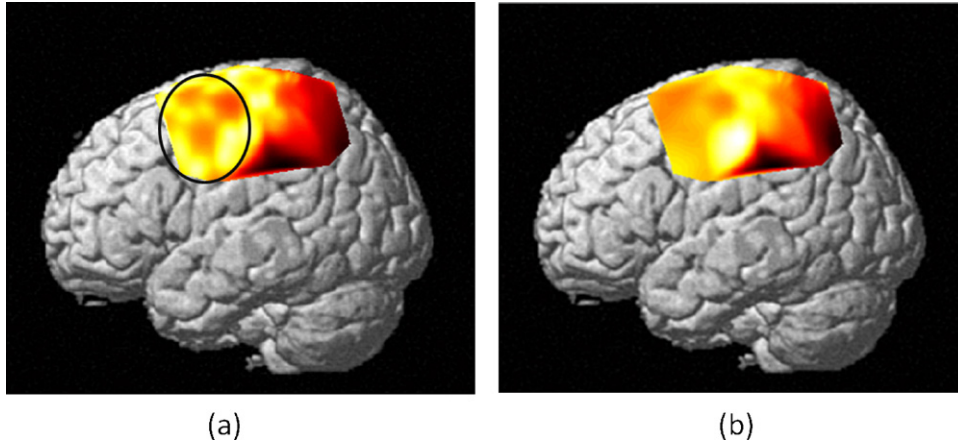


Fig. 3. Individual-level t maps: (a)–(c) activation maps of HbO, HbR, and HbT using Sun's tube formula (corrected p -value <0.05) and (d)–(f) activation maps of HbO, HbR, and HbT using the LKC-based expected EC method (corrected p -value <0.05).

Table 3Comparison of \mathcal{L}_2 and κ_0 and the corresponding thresholds for Sun's tube formula and LKC-based expected EC with $\rho_2(t)$ (corrected p -value <0.05).

	κ_0	\mathcal{L}_2	Threshold-tube	Threshold-EC	Difference
HbO	19.84	19.85	2.97	3.04	0.07
HbR	33.02	33.03	3.15	3.25	0.10
HbT	16.58	16.60	2.90	2.97	0.06

**Fig. 4.** Individual t map of a subject: (a) before modification of Σ_l (Eq. (11)); (b) after modification of Σ_l using Eq. (12). The ellipse represents the area with bee-hive like artifacts in individual t map.

nearly identical, so the difference in threshold mainly comes from different EC density functions. As expected by theory, the threshold of the LKC-based expected EC method is a little higher than that of Sun's tube formula due to the difference in t and Gaussian field. However, the threshold difference is so small that the activation maps produced by these two methods are similar as shown in Fig. 3. Note that for both correction methods, the activation maps are all around the primary motor cortex. More specifically, Figs. 3(a)–(c) shows the activation maps of HbO, HbR, and HbT, with p -values corrected by Sun's tube formula (corrected $p < 0.05$). Figs. 3(d)–(f) shows the activation maps of HbO, HbR, and HbT corrected by the LKC-based expected EC (corrected $p < 0.05$). In the right finger tapping task, the main target area is the primary motor cortex (BA 4). The equivalence between tube and EC are consistently observed for other individual data (results are not shown).

Furthermore, for some subjects, a bee-hive-like artifacts due to optode geometry used to be often observed in the individual t maps (Fig. 4(a)). After modifying Σ_l in Eq. (11) using Eq. (12), the artifact disappears (Fig. 4(b)). This indicates that incorporating channel-wise least-square residual correlation is very important to obtain more reasonable t -maps.

5. Discussion

In this paper, we found that the residual signals at each channel still show significant correlation. There may be several causes for this correlation. First, the design matrix is not sufficient to capture all activation patterns, so the least-square residual signals may be a biased estimate of true noise components, so they still have synchronous signal components. To compensate for this, a more elaborate design matrix may be needed to capture all temporal dynamics, which is beyond the scope of this paper. Second, the global synchronous dynamics may exist in fNIRS due to vascular response or skin blood flow. Recently, there have been some reports that fNIRS signal contains global vascular response arising from the blood flow and oxidative metabolism (Tong and Frederick, 2010; Gagnon et al., 2011). Therefore, the fNIRS signals at different channels may be highly correlated, which may lead to high

correlation in least-square residuals. Finally, since the spatial resolution of fNIRS is very low compared to that of fMRI, the neural activation tends to blur. Hence, the span of activation may appear across a large area, which may make the channels correlated in terms of the least-square residual temporal dynamics.

6. Conclusion

In this paper, we report an implementation of a family-wise error rate using the LKC-based expected Euler characteristic for fNIRS data analysis. We showed that the result of individual t random field produced by Sun's tube formula coincides with that produced by LKC-based expected EC method by incorporating channel-wise least-square residual correlation. After this modification, the beehive-like artifact, if any, disappears in t maps. The results in this paper supplement the existing NIRS-SPM toolbox.

Acknowledgements

This study was supported by a Korea Science and Engineering Foundation (KOSEF) grant funded by the Korea Government (MEST) (No. 2010-0000855).

Appendix A.

We derived the detailed process of estimation of LKC-based EC for individual analysis in fNIRS.

For a individual-level GLM, $\mathbf{y}_l(r) = \mathbf{X}\boldsymbol{\alpha}_l(r) + \boldsymbol{\epsilon}_l(r)$, the corresponding least-square residual is

$$\mathbf{r}_l(r) = \mathbf{y}_l(r) - \mathbf{X}\mathbf{X}^\dagger \mathbf{y}_l(r) = \mathbf{R}_x \mathbf{y}_l(r),$$

and the corresponding normalized residual is

$$\mathbf{Q}_l(r) = \frac{\mathbf{r}_l(r)}{\|\mathbf{r}_l(r)\|} = \frac{\mathbf{R}_x \mathbf{y}_l(r)}{\|\mathbf{R}_x \mathbf{y}_l(r)\|}.$$

Let

$$\mathbf{S}_l(r) = \nabla \mathbf{Q}_l(r) = \begin{bmatrix} \frac{\partial \mathbf{Q}_l(r)}{\partial x} & \frac{\partial \mathbf{Q}_l(r)}{\partial y} \end{bmatrix},$$

where

$$\begin{aligned} \frac{\partial \mathbf{Q}_l(r)}{\partial x} &= \frac{\partial(\mathbf{R}_x \mathbf{y}_l(r)) / (\|\mathbf{R}_x \mathbf{y}_l(r)\|)}{\partial x} \\ &= \frac{\mathbf{R}_x \frac{\partial \mathbf{y}_l(r)}{\partial x} \|\mathbf{R}_x \mathbf{y}_l(r)\| - \mathbf{R}_x \mathbf{y}_l(r) (\partial \|\mathbf{R}_x \mathbf{y}_l(r)\| / (\partial x))}{\|\mathbf{R}_x \mathbf{y}_l(r)\|^2}. \end{aligned}$$

and

$$\begin{aligned} \frac{\partial \mathbf{Q}_l(r)}{\partial y} &= \frac{\partial(\mathbf{R}_x \mathbf{y}_l(r)) / (\|\mathbf{R}_x \mathbf{y}_l(r)\|)}{\partial y} \\ &= \frac{\mathbf{R}_x (\partial \mathbf{y}_l(r) / (\partial y)) \|\mathbf{R}_x \mathbf{y}_l(r)\| - \mathbf{R}_x \mathbf{y}_l(r) (\partial \|\mathbf{R}_x \mathbf{y}_l(r)\| / (\partial y))}{\|\mathbf{R}_x \mathbf{y}_l(r)\|^2}. \end{aligned}$$

As shown in Appendix B, $\mathbf{y}_l(r) = (\mathbf{b}_l(r)^T \otimes \mathbf{I}_N) \mathbf{y}_l$, so

$$\begin{aligned} \frac{\partial \mathbf{y}_l(r)}{\partial x} &= \frac{\partial((\mathbf{b}_l(r)^T \otimes \mathbf{I}_N) \mathbf{y}_l)}{\partial x} = \left(\frac{\partial \mathbf{b}_l(r)^T}{\partial x} \otimes \mathbf{I}_N \right) \mathbf{y}_l, \\ \frac{\partial \mathbf{y}_l(r)}{\partial y} &= \frac{\partial((\mathbf{b}_l(r)^T \otimes \mathbf{I}_N) \mathbf{y}_l)}{\partial y} = \left(\frac{\partial \mathbf{b}_l(r)^T}{\partial y} \otimes \mathbf{I}_N \right) \mathbf{y}_l. \end{aligned}$$

and

$$\begin{aligned} \frac{\partial \|\mathbf{R}_x \mathbf{y}_l(r)\|}{\partial x} &= \frac{(\partial \mathbf{y}_l^T(r)) / (\partial x) \mathbf{R}_x \mathbf{y}_l(r) + \mathbf{y}_l^T(r) \mathbf{R}_x (\partial \mathbf{y}_l(r) / (\partial x))}{2 \|\mathbf{R}_x \mathbf{y}_l(r)\|} \\ \frac{\partial \|\mathbf{R}_x \mathbf{y}_l(r)\|}{\partial y} &= \frac{(\partial \mathbf{y}_l^T(r)) / (\partial y) \mathbf{R}_x \mathbf{y}_l(r) + \mathbf{y}_l^T(r) \mathbf{R}_x (\partial \mathbf{y}_l(r) / (\partial y))}{2 \|\mathbf{R}_x \mathbf{y}_l(r)\|}. \end{aligned}$$

Since the basis function $\mathbf{b}_l(r)$ is given explicitly, the calculation of its derivatives can be done efficiently, so we can obtain the quantities for LKC-formula very easily.

Then, the estimation of 2-dimensional LKC of Φ_l is

$$\hat{\mathcal{L}}_2(\Phi_l) = \sum_{r \in \Phi_l} \det(\mathbf{S}_l(r)^T \mathbf{S}_l(r))^{1/2},$$

which makes the largest contribution of the p -value approximation (Taylor and Worsley, 2008). Since we have estimated $\hat{\mathcal{L}}_2(\Phi_l)$, assuming that the Φ_l is a disk, we can calculate $\hat{\mathcal{L}}_1(\Phi)$ and $\hat{\mathcal{L}}_0(\Phi)$ as follows (Taylor and Worsley, 2008):

$$\hat{\mathcal{L}}_0(\Phi) = 1, \quad \hat{\mathcal{L}}_1(\Phi) = \pi r.$$

$$\text{where } r = \sqrt{\hat{\mathcal{L}}_2(\Phi_l) / \pi}.$$

Appendix B.

In Ye et al. (2009), the individual-level GLM before interpolation is as follows:

$$\mathbf{y}_l = (\mathbf{I}_K \otimes \mathbf{X}) \boldsymbol{\beta}_l + \boldsymbol{\epsilon}_l,$$

where K denotes the number of channels, and $\boldsymbol{\beta}_l \in \mathbb{R}^{KM}$ are individual-level parameters for all channels. The interpolated time series at any position r can be derived as follows:

$$\begin{aligned} \mathbf{y}_l(r) &= (\mathbf{b}_l(r)^T \otimes \mathbf{I}_N) \mathbf{y}_l = (\mathbf{b}_l(r)^T \otimes \mathbf{I}_N) (\mathbf{I}_K \otimes \mathbf{X}) \boldsymbol{\beta}_l + \boldsymbol{\epsilon}_l(r) \\ &= (\mathbf{b}_l(r)^T \otimes \mathbf{X}) \boldsymbol{\beta}_l + \boldsymbol{\epsilon}_l(r) \\ &= (\mathbf{1} \otimes \mathbf{X}) (\mathbf{b}_l(r)^T \otimes \mathbf{I}_M) \boldsymbol{\beta}_l + \boldsymbol{\epsilon}_l(r) \\ &= \mathbf{X} (\mathbf{b}_l(r)^T \otimes \mathbf{I}_M) \boldsymbol{\beta}_l + \boldsymbol{\epsilon}_l(r) \\ &= \mathbf{X} \boldsymbol{\alpha}_l(r) + \boldsymbol{\epsilon}_l(r), \end{aligned}$$

where $\mathbf{b}_l(r)$ is the interpolated kernel and $\boldsymbol{\epsilon}_l(r) = (\mathbf{b}_l(r)^T \otimes \mathbf{I}_N) \boldsymbol{\epsilon}_l$. This implies that at any interpolated point, the same design matrix can be used for GLM.

Moreover, the covariance of $\mathbf{C}_{\boldsymbol{\epsilon}_l(r)}$ is as follows:

$$\begin{aligned} \mathbf{C}_{\boldsymbol{\epsilon}_l(r)} &= (\mathbf{b}_l(r)^T \otimes \mathbf{I}_N) \mathbf{C}_{\boldsymbol{\epsilon}_l} (\mathbf{b}_l(r) \otimes \mathbf{I}_N) \\ &= (\mathbf{b}_l(r)^T \otimes \mathbf{I}_N) (\boldsymbol{\Sigma}_l \otimes \boldsymbol{\Lambda}_l) (\mathbf{b}_l(r) \otimes \mathbf{I}_N) \\ &= (\mathbf{b}_l(r)^T \boldsymbol{\Sigma}_l \mathbf{b}_l(r)) \otimes \boldsymbol{\Lambda}_l. \end{aligned}$$

References

- Adler R, Taylor J. Random fields and geometry. Springer Verlag; 2007.
- Boas D, Gaudette T, Strangman G, Cheng X, Marota J, Mandeville J. The accuracy of near infrared spectroscopy and imaging during focal changes in cerebral hemodynamics. *NeuroImage* 2001;13(1):76–90.
- Boas D, Strangman G, Culver J, Hoge R, Jasdzewski G, Poldrack R, et al. Can the cerebral metabolic rate of oxygen be estimated with near-infrared spectroscopy? *Phys Med Biol* 2003;48(15):2405–18.
- Cope M, Delpy D. System for long-term measurement of cerebral blood and tissue oxygenation on newborn infants by near infra-red transillumination. *Med Biol Eng Comput* 1988;26(3):289–94.
- Friston K, Ashburner J, Kiebel S, Nichols T, Penny W, editors. Statistical parametric mapping: the analysis of functional brain images. Academic Press; 2007.
- Gagnon L, Perdue K, Greve D, Goldenholz D, Kaskhedikar G, Boas D. Improved recovery of the hemodynamic response in diffuse optical imaging using short optode separations and state-space modeling. *NeuroImage* 2011;56(3):1362–71.
- Jang K, Tak S, Jung J, Jang J, Jeong Y, Ye J. Wavelet minimum description length detrending for near-infrared spectroscopy. *J Biomed Opt* 2009;14(3):034004.
- Koh P, Glaser D, Flandin G, Kiebel S, Butterworth B, Maki A, Delpy D, et al. Functional optical signal analysis: a software tool for near-infrared spectroscopy data processing incorporating statistical parametric mapping. *J Biomed Opt* 2007;12(6):064010.
- Mehagnoul-Schippier D, van der Kallen B, Colier W, van der Sluijs M, van Erning L, Thijssen H, et al. Simultaneous measurements of cerebral oxygenation changes during brain activation by near-infrared spectroscopy and functional magnetic resonance imaging in healthy young and elderly subjects. *Human Brain Map* 2002;16(1):14–23.
- Plichta M, Heinzel S, Ehliis A, Pauli P, Fallgatter A. Model-based analysis of rapid event-related functional near-infrared spectroscopy (NIRS) data: A parametric validation study. *NeuroImage* 2007;35(2):625–34.
- Schroeter ML, Bucheler MM, Muller K, Uludag K, Obrig H, Lohmann G, et al. Towards a standard analysis for functional near-infrared imaging. *NeuroImage* 2004;21:283–90.
- Singh A, Dan I. Exploring the false discovery rate in multichannel NIRS. *NeuroImage* 2006;33(2):542–9.
- Takemura A, Kuriki S. Maximum of Gaussian field on piecewise smooth domain: Equivalence of tube method and Euler characteristic method. *Ann Appl Prob* 2002;12:768–96.
- Takemura A, Kuriki S. Tail probability via the tube formula when the critical radius is zero. *Bernoulli* 2003;9(3):535–58.
- Taylor J, Worsley K. Detecting sparse signals in random fields, with an application to brain mapping. *J Am Stat Assoc* 2007;102(479):913–28.
- Taylor J, Worsley K. Random fields of multivariate test statistics, with applications to shape analysis. *Ann Stat* 2008;36(1):1–27.
- Tong Y, Frederick B. Time lag dependent multimodal processing of concurrent fMRI and near-infrared spectroscopy (NIRS) data suggests a global circulatory origin for low-frequency oscillation signals in human brain. *NeuroImage* 2010;53(2):553–64.
- Toronov V, Webb A, Choi J, Wolf M, Michalos A, Gratton E, et al. Investigation of human brain hemodynamics by simultaneous near-infrared spectroscopy and functional magnetic resonance imaging. *Med Phys* 2001;28:521.
- Villringer A, Dirnagl U. Coupling of brain activity and cerebral blood flow: basis of functional neuroimaging. *Cerebrovas Brain Metabol Rev* 1995;7(3):240.
- Worsley K. Boundary corrections for the expected Euler characteristic of excursion sets of random fields, with an application to astrophysics. *Adv Appl Prob* 1995;27(4):943–59.
- Worsley K, Andermann M, Koulis T, MacDonald D, Evans A. Detecting changes in nonisotropic images. *Human Brain Map* 1999;8:2–3, :98–101.
- Ye J, Moulin P, Bresler Y. Asymptotic global confidence regions for 3-D parametric shape estimation in inverse problems. *IEEE Trans Image Process* 2006;15(10):2904–19.
- Ye J, Tak S, Jang K, Jung J, Jang J. NIRS-SPM: statistical parametric mapping for near-infrared spectroscopy. *NeuroImage* 2009;44(2):428–47.